Possible sources of coercivity in thin films of amorphous rare earth-transition metal alloys

Roscoe Giles and Masud Mansuripur

Possible sources of coercivity in thin films of amorphous rare earth-transition metal alloys

Roscoe Giles
College of Engineering, Boston University, Boston, Massachusetts 02215

Masud Mansuripur
Optical Sciences Center, University of Arizona, Tucson, Arizona 85721

Computer simulations of a two-dimensional lattice of magnetic dipoles are performed on the Connection Machine. The lattice is a discrete model for thin films of amorphous rare earth-transition metal alloys, which have application as the storage media in erasable optical data storage systems. In these simulations the dipoles follow the dynamic equation of Landau–Lifshitz–Gilbert under the influence of an effective field arising from local anisotropy, near-neighbor exchange, classical dipole–dipole interactions, and an externally applied field. The effect of random axis anisotropy on the coercive field is studied and it is found that the fields required for the nucleation of reverse-magnetized domains are generally higher than those observed in the experiments. Various "defects" are then introduced in the magnetic state of the lattice and the values of coercivity corresponding to different types, sizes, and strengths of these "defects" are computed. It was found, for instance, that voids have insignificant effects on the value of the coercive field, but that reverse-magnetized seeds of nucleation, formed and stabilized in areas with large local anisotropy, can substantially reduce the coercivity.

INTRODUCTION

Magnetization reversal in thin films of amorphous rare earth-transition metal alloys is of considerable importance in erasable optical data storage.[1-12] The success of thermomagnetic recording and erasure depends on the reliable and repeatable reversal of magnetization in micron-size areas within the storage medium. A major factor entering the thermomagnetic process is the coercivity of the magnetic medium and its temperature dependence. The purpose of this paper is to investigate coercivity at the submicrometer scale using large scale computer simulations. There exists a substantial literature addressing the various aspects and mechanisms of coercivity in thin films; the interested reader may consult Refs. 13–26.

Our computer simulations were performed on a two-dimensional hexagonal lattice of magnetic dipoles following the Landau–Lifshitz–Gilbert equation. In addition to interacting with an externally applied field, the dipoles were subject to effective fields arising from local uniaxial anisotropy, nearest neighbor exchange, and long range dipole–dipole interactions. Details of the micromagnetic model have been previously published[27-32] and will not be repeated here. Suffice it to say that the massive parallelism of the Connection Machine on which these simulations were performed, together with the fast Fourier transform algorithm,[30,31] which was used to compute the demagnetizing fields, enabled us to accurately simulate a large (256×256) hexagonal lattice of dipoles. Since the lattice constant was chosen to be 10 Å in these simulations, the total area of the lattice corresponds to a section of the magnetic film with dimensions 0.256×0.222 μm.

The reported results in this paper utilize a color coding scheme for representing the state of magnetization. Since the magnitude of the magnetization vector **m** will be fixed throughout the lattice, the *color sphere* is used to represent its local orientation. The color sphere is white at its north pole, black at its south pole, and covers the visible spectrum on its equator in the manner shown in Fig. 1. As one moves from the equator to the north pole on a great circle, the color pales, i.e., it mixes with increasing amounts of white, until it becomes white at the pole. Moving toward the south pole has the opposite effect as the color mixes with increasing amounts of black. Thus when the magnetization vector at a given site is perpendicular to the plane of the lattice and along the positive (negative) Z axis, its corresponding pixel will be white (black). For **m** in the plane of the lattice the pixel is red when pointing along $+X$, light green along $+Y$, blue along $-X$, and purple along $-Y$. In the same manner, other orientations of **m** map onto the corresponding color on the color sphere.

The organization of this paper is as follows. In Sec. I we describe the nucleation coercivity and the influence of random axis anisotropy and/or defects on nucleation. Section II is devoted to the structure and motion of domain walls, where we discuss certain aspects of wall coercivity. Also presented in this section are several results concerning demagnetization that involve wall motion. Concluding re-
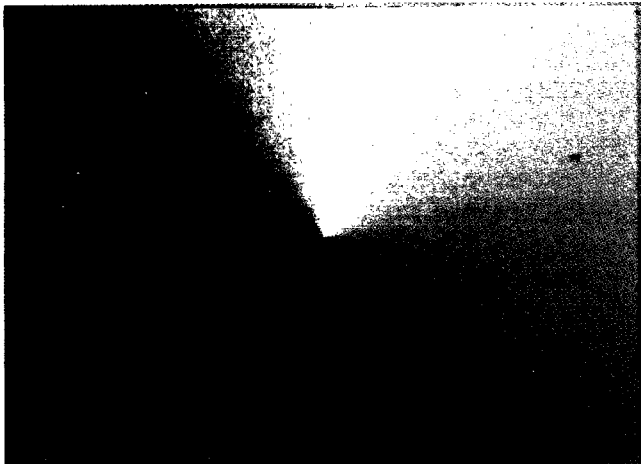
FIG. 1. The color circle shown in this figure may be used to encode the direction of magnetization in the plane of the lattice. In this scheme a red pixel is associated with local magnetization direction along $+X$, light green corresponds to $+Y$, blue to $-X$, and purple to $-Y$. When a vector is not completely in the plane of the lattice, but has a perpendicular component along $+Z$ (or $-Z$), its associated color is obtained by mixing the color of its in-plane component with a certain amount of white (or black), the strength of white (or black) depending on the magnitude of the vertical component. A vector fully aligned with the $+Z$ direction is shown by a white pixel, while a vector in the $-Z$ direction is displayed as black.

marks are the subject of Sec. III. A generalized version of the Stoner–Wohlfarth theory of magnetization reversal by coherent rotation is described in the Appendix. We compare the predictions of this model with some of the results obtained by computer simulation, and show the excellent agreement between them.

I. NUCLEATION COERCIVITY, RANDOM AXIS ANISOTROPY, AND VARIOUS DEFECT MECHANISMS

In order to gain an understanding of the possible sources of nucleation coercivity, we chose a lattice with the following set of parameters: saturation magnetization $M_s = 100$ emu/cm^3, anisotropy energy constant $K_u = 10^6$ erg/cm^3, exchange stiffness coefficient $A_x = 10^{-7}$ erg/cm, film thickness $h = 500$ Å, damping coefficient $\alpha = 0.5$, and gyromagnetic ratio $\gamma = -10^7$ Hz/Oe. This set of parameters shall be referred to as the set corresponding to the *basic sample*. The axes of anisotropy were distributed randomly and independently among the lattice cells in such a way as to keep their deviation from the Z axis below a certain maximum angle Θ. In the following discussions Θ will be referred to as the cone angle.

The first set of simulations concerned the relationship between the coercive field H_c and the cone angle Θ. Hysteresis loops were traced for several cone angles in the range of 20°–45°. The loops were always square (i.e., nucleation coercivity dominated the wall motion coercivity) and H_c decreased monotonically from 17 kOe at $\Theta = 20°$ to 12.5 kOe at $\Theta = 45°$. H_c for a given cone angle showed a slight dependence on the choice of seed for the random number generator. For instance, in the case of $\Theta = 45°$, different seeds gave rise to coercivities between 12.5 and 12.80 kOe. Similar variations in the nucleation coercivity of real materials can be expected, provided that small areas of these films are subjected to the external field. Alternatively, the dependence of the computed coercivity on the random

number seed should disappear when the simulated lattice becomes sufficiently large.

Frame (a) in Fig. 2 shows the initial phase of the reversal process (i.e., the nucleation phase) for the basic sample with $\Theta = 45°$ under an applied field of $H_{ext} = 12.6$ kOe, which happens to be just above the coercive field for the sample. The nucleation site is in the lower central part

(a)

(b)

(c)

FIG. 2. Early stage of nucleation for three samples with $M_s = 100$ emu/cm^3, $K_u = 10^6$ erg/cm^3, $h = 500$ Å, and cone angle $\Theta = 45°$. The applied field in all cases is 12.6 kOe. In frame (a) the sample has exchange stiffness coefficient $A_x = 10^{-7}$ erg/cm. For the sample in frame (b) the exchange parameter is $A_x = 0.8 \times 10^{-7}$, while frame (c) represents a sample with $A_x = 0.6 \times 10^{-7}$.
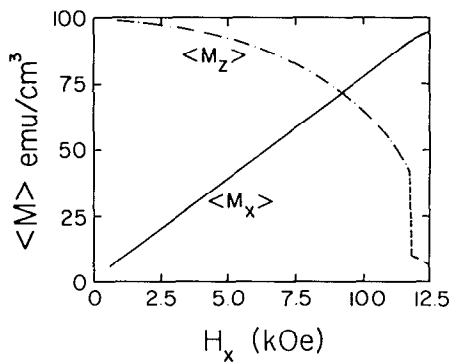
FIG. 3. Average components of magnetization along X and Z versus magnitude of the in-plane applied field H_x. The parameters of the lattice are those of the basic sample with $\Theta = 45°$, and the system is relaxed to the steady state for each value of the applied field.

of the frame and its periodic continuation, due to the boundary conditions and the hexagonal symmetry of the lattice, appears at the upper left corner of the frame.

In order to understand the relative significance of anisotropy and exchange in the nucleation process, we varied the exchange parameter while keeping all other parameters (including the random number seed) fixed at their previous values corresponding to frame (a). Frame (b) shows the early nucleation stage for a sample whose exchange parameter A_x has been reduced to 80% of the original value. Within the accuracy of calculations, the value of coercivity for this sample was found to be the same as the original sample's coercivity, although the nucleation site at the applied field of 12.6 kOe appears to be different. Further reduction of A_x to 60% of its original value does not make any difference either [see frame (c)]; the coercivity remains the same and even the site of nucleation remains the same as in frame (b). From the above observations we conclude that nucleation coercivity is controlled by the anisotropy field $H_k = 2K_u/M_s$ as well as by the spread in the

distribution of the axes of anisotropy. The nucleation site must have an "average" anisotropy field close to the applied field (i.e., $H_{ext} \approx 2\langle K_u \rangle / M_s - 4\pi M_s$), but the strength of exchange is not of primary significance in this respect.

It must be emphasized at this point that K_u, as used in our model, is different from the bulk anisotropy as measured for a real magnetic film by, say, torque magnetometry. Bulk anisotropy should be denoted by $\langle K_u \rangle$, where brackets indicate spatial averaging, whereas K_u itself represents the strength of local anisotropy associated with each dipole. Thus when the cone angle Θ is increased while K_u is being kept constant, the bulk anisotropy $\langle K_u \rangle$ should decrease.

To clarify the distinction between K_u and $\langle K_u \rangle$, we simulated an experiment in which the bulk anisotropy of the sample could be measured. In the experiment, one applies an in-plane field, say along the X axis, and monitors the normal component of magnetization $\langle M_z \rangle$ as a function of the strength of the applied field. The value of bulk anisotropy $\langle K_u \rangle$ is then obtained from the curvature of the plot of $\langle M_z \rangle$ vs H_x (Ref. 33). Figure 3 shows plots of $\langle M_x \rangle$ and $\langle M_z \rangle$ as functions of H_x, obtained by simulation for the basic sample with cone angle $\Theta = 45°$. For each value of H_x the lattice was relaxed to the steady-state before $\langle M_x \rangle$ and $\langle M_z \rangle$ were computed. It is seen in this figure that for values of H_x below 12 kOe the magnetic moments move coherently and reversibly toward the direction of the applied field. Using either the slope of $\langle M_x \rangle$ or the curvature of $\langle M_z \rangle$ it is rather straightforward to show that

$$2\langle K_u \rangle / M_s - 4\pi M_s \simeq 13 \text{ kOe},$$

in agreement with our previous results concerning the nucleation field.

Although not relevant to the present discussion, it is interesting to know what happens when H_x in the preceding experiment is increased beyond the critical value of 12 kOe. At the critical field some moments flip over to the other side and create regions of reverse magnetization. Frame (a) in Fig. 4 shows the distribution of M_z across the
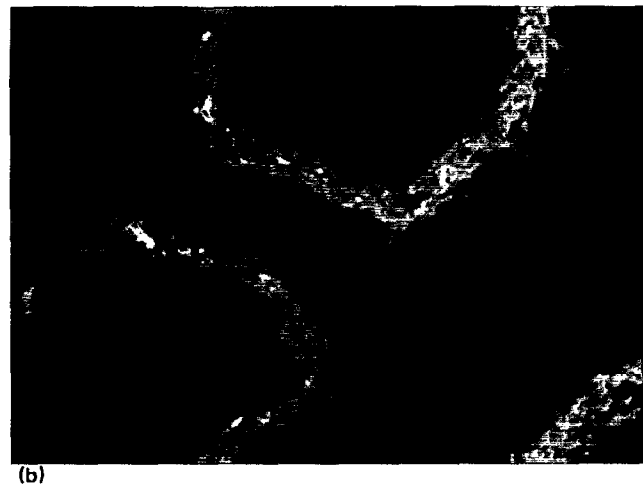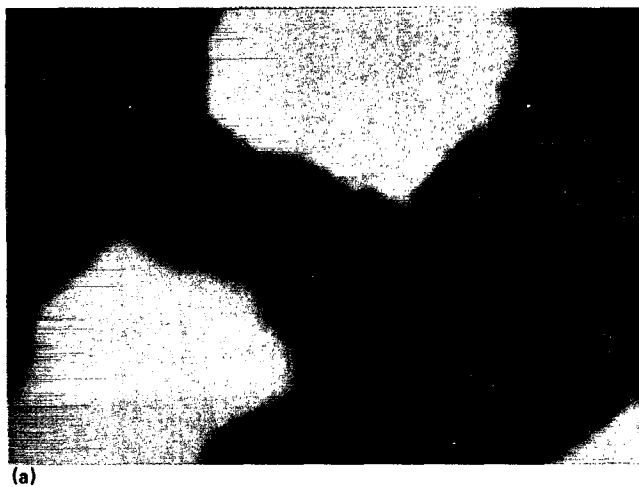

(a)

(b)

FIG. 4. Distribution of M_z (a) and exchange energy (b) across the lattice in the steady state, under the applied in-plane field $H_x = 12$ kOe. The color coding scheme here differs from that used in all the other figures of the paper, and is applicable only when a scalar function (such as the local value of M_z across the lattice) is to be displayed. In this scheme the color red is assigned to the minimum value of the function, while the color purple is used to represent the maximum value. All the other values are then mapped onto the color circle in a linear fashion, starting from red and moving counterclockwise to purple.
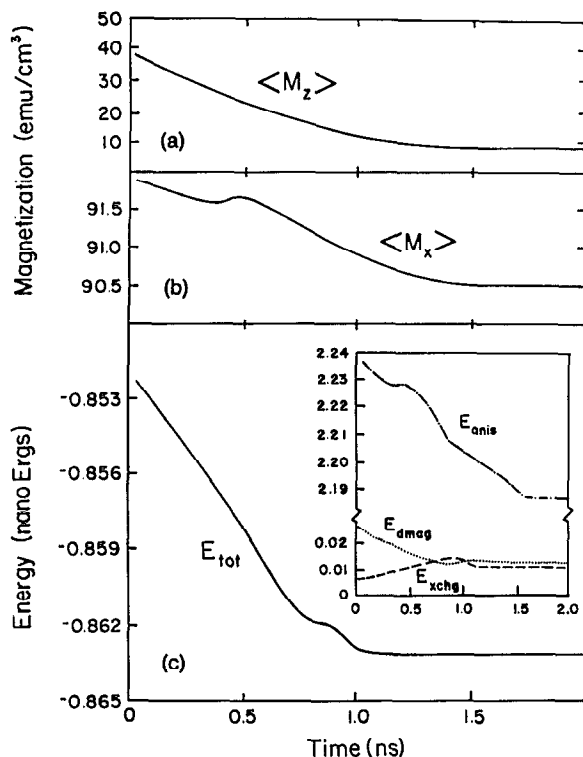
FIG. 5. Average magnetization and energy during the relaxation process that leads to the steady state in Fig. 4. (a) $\langle M_z \rangle$ versus time. (b) $\langle M_x \rangle$ versus time. (c) Total energy of the lattice versus time. The inset shows separate plots of exchange, anisotropy, and demagnetization energies.

lattice in the steady state, under the applied field $H_x = 12$ kOe. (Note: The color code used for Fig. 4 differs from the code described in the Introduction and used for all the other figures in this paper. The caption to Fig. 4 describes this particular coloring scheme.) The blue regions in Fig. 4(a) have a small positive value of M_z, while M_z for the yellow regions is small and negative. The same coloring scheme is also used in frame (b) to show the distribution of exchange

energy in the steady state. Plots of the exchange energy distribution emphasize domain walls and enhance regions with rapid spatial variation of magnetization. Behavior of the average magnetization and energy during the relaxation process under the applied field $H_x = 12$ kOe are shown in Fig. 5. The rapid drop in $\langle M_z \rangle$ is due to the onset of demagnetization, which also causes a small drop in $\langle M_x \rangle$. The reduction in energy is attributable to a lowered anisotropy energy, as is readily observed from the inset in Fig. 5(c).

Going back to the subject of magnetization reversal under a perpendicularly applied field, it appears that the nucleation coercivity is always about $2\langle K_u \rangle / M_s$. On the other hand, one can make the following assumptions about a real sample: (i) The bulk of the material has very little dispersion in its local easy axes, and (ii) only a few isolated submicron-size regions have large values of Θ. Under these circumstances $\langle K_u \rangle \simeq K_u$ while, at the same time, since nucleation takes place in regions of large dispersion, the resulting coercivity is significantly below $2\langle K_u \rangle / M_s$.

In contrast to these results, the experimentally observed values of coercivity for real samples (with parameters similar to those of the basic sample) are only a few kilo Oersteds. Nucleation in real materials therefore cannot be attributed to random axis anisotropy alone. We believe that the reveral process has its origins in what may be termed "defects," be they structural or magnetic in nature. Results of simulation studies pertaining to several different types of defects are outlined in the following subsections.

A. Defects of type 1

These defects are small regions of the sample from which the magnetic material has been removed and, as such, they may be characterized as voids. Figure 6 corresponds to a circular void with diameter $D = 500$ Å in the basic sample. Random axis anisotropy with a cone angle of $\Theta = 45°$ has also been assumed throughout the lattice. The simulation results indicate that, within the accuracy of calculations, the value of coercivity has been unaffected by the void (i.e., $H_c \simeq 12.6$ kOe). Due to the long range dipole–dipole interactions, however, the nucleation site has moved from the

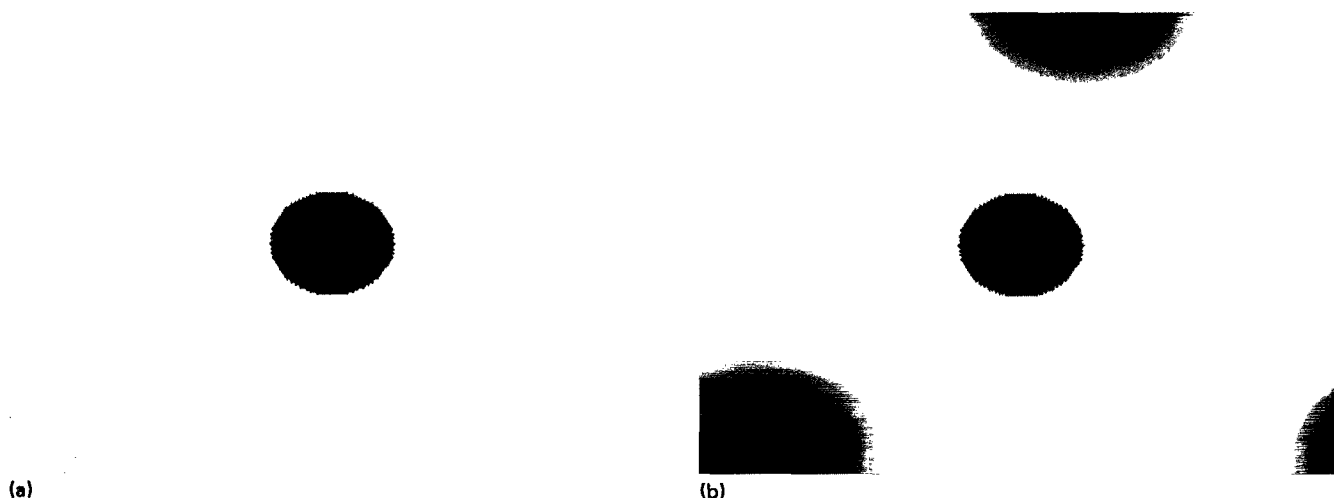(a)   (b)

FIG. 6. Nucleation in the basic sample with a defect of type 1 (void) at the center. (a) The state of magnetization of the lattice at an applied field of $H_{ext} = 12.5$ kOe, just below coercivity. (b) Nucleation and growth of a reverse magnetized domain under an applied field of $H_{ext} = 12.6$ kOe.

lower central part of the lattice in the absence of the void [see Fig. 2, frame (a)] to the lower left corner of the lattice in Fig. 6.

It should be noted that the assumed defect does not influence the magnetic properties of the void boundary; in particular, the saturation magnetization M_s, the anisotropy constant K_u, and the distribution of the anisotropy axes at the periphery of the void have been left intact. In reality, one expects the presence of the void to alter these parameters, albeit to an extent which is not well understood at the present time. Thus, despite the above result, the possibility that real voids could act as nucleation centers should not be completely ruled out.

B. Defects of type 2

The second type of defect is a small region with large anisotropy constant K_u and with reverse magnetization. In simulation results displayed in Fig. 7 the basic sample had the same axes of anisotropy as in the preceding cases, but
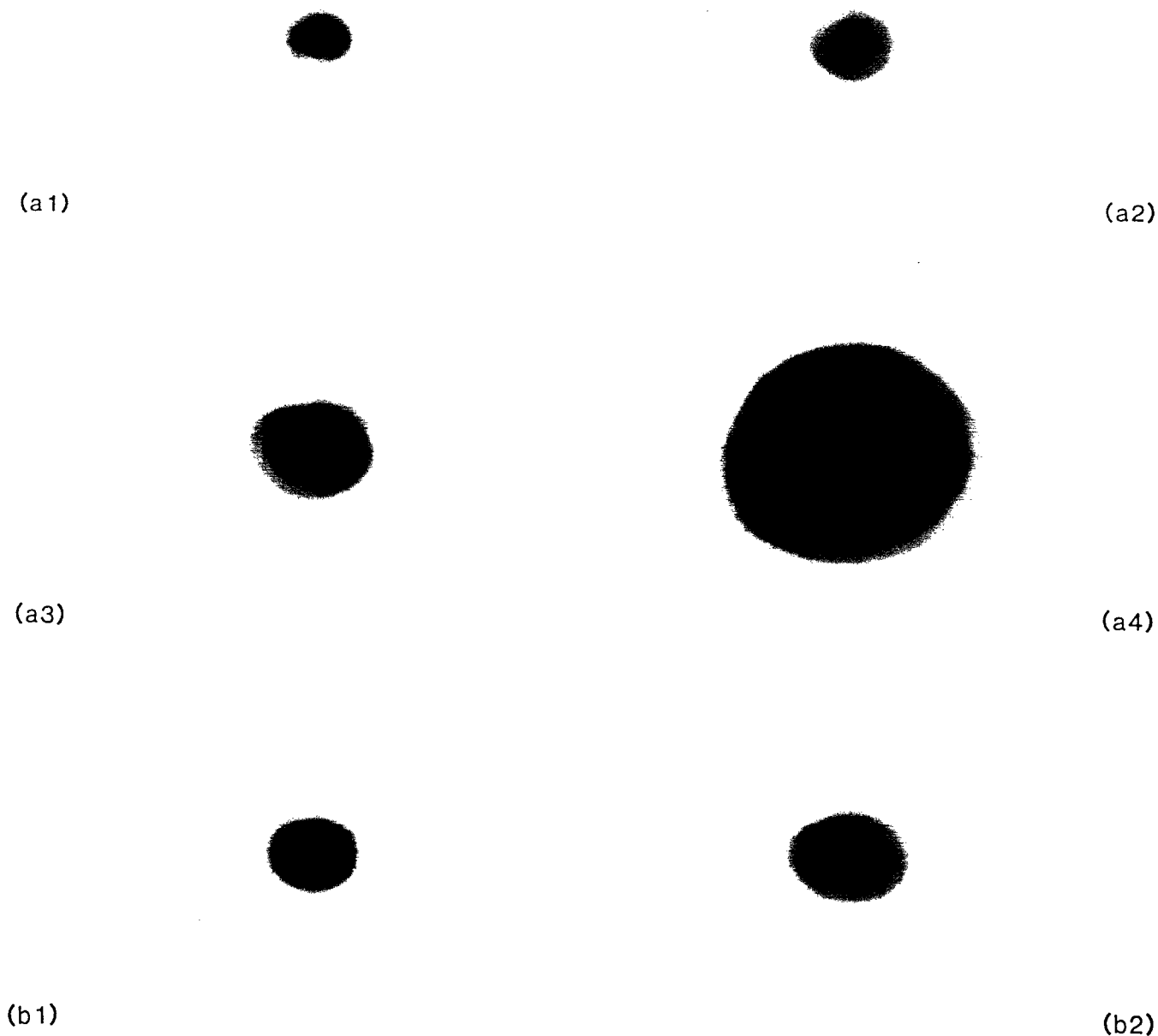
(a1)

(a2)

(a3)

(a4)

(b1)

(b2)

FIG. 7. Nucleation in the basic sample with a defect of type 2. (a1) A defect with diameter $D = 200$ Å in the remanent state. (a2) Growth of the initial domain under an applied field of $H_{ext} = 3.46$ kOe. The state shown in this frame corresponds to $t = 189$ ps after the application of the field. (a3) Continued growth under $H_{ext} = 3.46$ kOe. The state shown here was obtained at $= 500$ ps. (a4) State of the lattice under $H_{ext} = 3.46$ kOe at $t = 797$ ps. (b1) Defect of initial diameter $D = 300$ Å in the remanent state. (b2) Growth of the initial domain under the applied field of $H_{ext} = 1.98$ kOe.

K_u within the defective region at the center of the lattice was increased tenfold to 10^7 erg/cm^3. A defect with diameter $D = 100$ Å was not stable in the remanent state and collapsed. A defect with 200 Å diameter, however, was stable; the remanent pattern of magnetization in this case is shown in frame (a1). The required field for the expansion of this defect is only 3.45 kOe, which is substantially below the value of coercivity for the same sample without defect (12.57 kOe). Frames (a2), (a3), and (a4) in Fig. 7 show the growth of this nucleus under the applied field of 3.46 kOe. Similar results were obtained for a defect diameter of 300 Å, as shown in frames (b1) and (b2). The coercivity in this case was 1.98 kOe. When the defect diameter was increased to 500 Å, the coercivity dropped to 1.28 kOe. These results clearly indicate that defects of type 2 can control the coercivity in a major way.

The preceding numerical results are in good agreement with predictions based on a relatively simple theory. Consider a circular domain of radius r in a film of thickness h, saturation magnetization M_s, and domain wall energy density σ_w. Let an external field H_{ext} be applied perpendicular to the plane of the film, favoring the direction of magnetization inside the domain. Assuming that $0 \ll r \lesssim h$, the energy of the system (relative to the saturated state with no domains) is written

$$E \simeq -2\pi r^2 h M_s H_{ext} + 2\pi r h \sigma_w$$
$$- \pi(r + 1.5h)^2 h (2\pi M_s^2). \qquad (1)$$

The approximation in Eq. (1) is caused by the last term, which corresponds to demagnetization. The implicit assumption here is that, upon the formation of the domain, the demagnetizing field in and around the domain within a radius of $r + 1.5h$ vanishes. Of course, if the domain radius r is much less than the film thickness h, the above approximation fails, because in that case the demagnetizing field cannot be reduced in a substantial way in locations that are as far away as $r + 1.5h$ from the center. Similarly, when r happens to be much larger than h, the approximation fails once again because now the demagnetizing field is not diminished within the domain; only the annular region between $r - 1.5h$ and $r + 1.5h$ may now be assumed to have zero demagnetizing field. These are the reasons behind the restrictions imposed on Eq. (1).

When H_{ext} is sufficiently small, the net pressure on the wall will be inwards and the domain tends to collapse (except that in the case of interest here the large value of K_u within the domain opposes this tendency). At the onset of expansion, when H_{ext} is large enough to begin to push the wall outwards, the net pressure is zero, that is, $dE/dr = 0$. One can readily derive the expression for the critical value of H_{ext} as follows:

$$H_{ext} = [\sigma_w - 2\pi(r + 1.5h)M_s^2]/2rM_s. \qquad (2)$$

Although in subsequent discussions the numerical value of σ_w will be obtained from the formula

$$\sigma_w = 4\sqrt{A_x K_u}, \qquad (3)$$
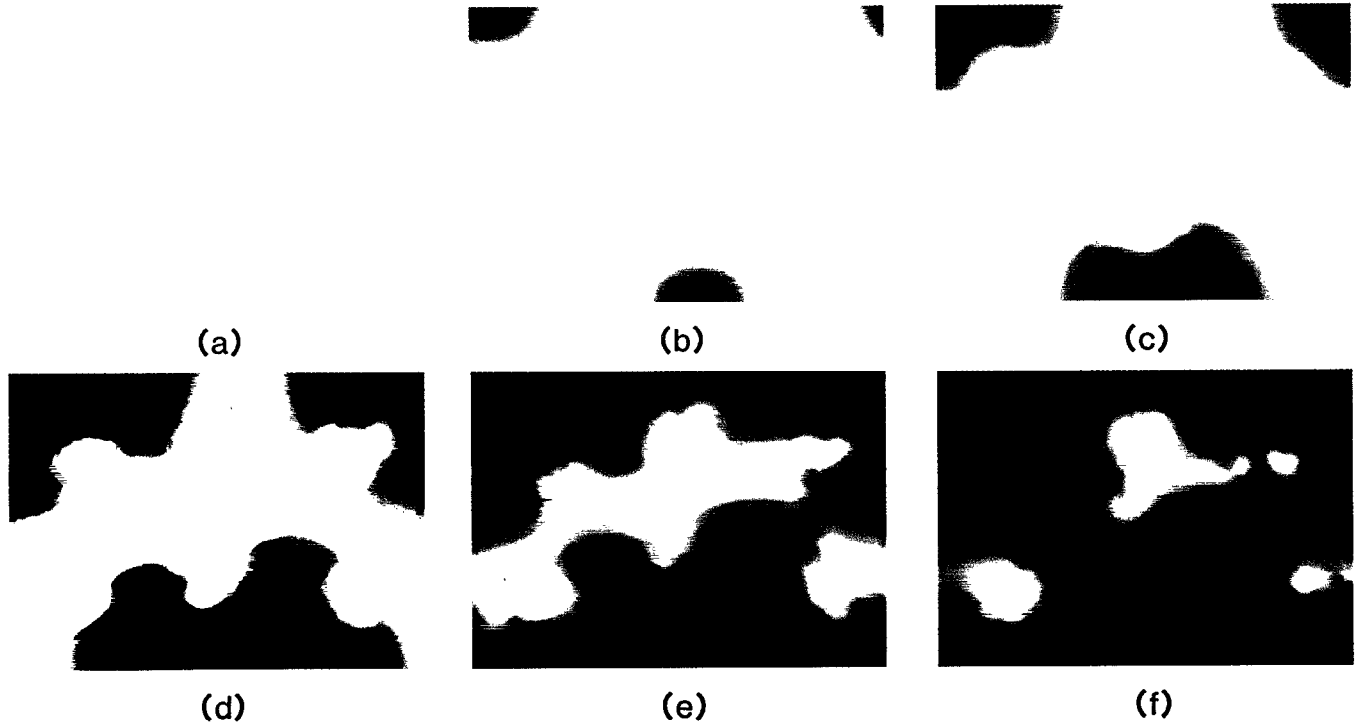

(a)   (b)   (c)

(d)   (e)   (f)

FIG. 8. Nucleation and growth in the basic sample with isolated regions of large anisotropy. Six small areas of diameter 400 Å within the lattice were assigned a value of K_u which was five times greater than K_u for the rest of the lattice. The magnetization of the entire lattice was then saturated and relaxed to the remanent state. Frame (a) shows the state of the lattice under $H_{ext} = 12.5$ kOe, just below coercivity. In frame (b) the applied field is 12.6 kOe and there is nucleation. Frame (c) shows how the growth of the initial nucleus is hampered by three of the defects. The remaining frames follow the growth process in time and show the way in which the magnetization manages to reverse the high K_u regions.

it should be remembered that, due to random anisotropy and the presence of vertical Bloch lines, the actual value of σ_w in our simulations is somewhat different from the value of 1.265 erg/cm^2 predicted by Eq. (3). For $r = 100$, 150, and 250 Å, corresponding to the simulated defects of type 2, the calculated coercivities from Eq. (2) are 3.65, 2.33, and 1.27 kOe, respectively.

Of course, regions with large K_u are not necessarily reverse magnetized in every situation. Consider, for instance, the case of a completely saturated sample with six regularly spaced defects shown in Fig. 8. The defects are cylindrical regions of diameter $D = 400$ Å and $K_u = 5 \times 10^6$ erg/cm^3. Otherwise, the lattice has parameters of the basic sample with cone angle $\Theta = 45°$. Frame (a) shows the state of the lattice under an applied field of $H_z = 12.5$ kOe, which is slightly below the coercivity for the sample. Frames (b)–(f) show the nucleation and growth of a reverse domain under the applied field of $H_z = 12.6$ kOe. Although the defects act as temporary barriers to the growing nucleus, the walls eventually sweep through the entire sample. At the end, the magnetization of the sample is fully saturated in the reverse direction, and defects of type 2 (which could have formed around the regions of high K_u) do not materialize.

In contrast to the preceding results, Fig. 9 shows a case where defects of type 2 with either polarity can be stable. In this case there are seven cylindrical regions of diameter $D = 200$ Å and $K_u = 10^7$ erg/cm^3. The central region is initially reverse magnetized and thus constitutes a defect of type 2. The rest of the sample is saturated along

$+ Z$ and then relaxed to the remanent state, as shown in frame (a). Under an external field $H_z = -3.5$ kOe (just above coercivity), the central nucleus expands and covers the rest of the sample with the exception of the high K_u regions. Frames (b)–(f) follow the growth process in time under the applied field. The six unreversed regions in frame (f) may now act as defects of type 2 for future reversals.

Finally, one must recognize that defects of type 2 are inherently unstable and could be eliminated by applying sufficiently large magnetic fields. The required field for destroying a particular defect, of course, depends on its size and on the strength of its anisotropy. In reality, if coercivity is controlled by this type of defect, then one expects to find a dependence of H_c on the history of saturation and, in particular, on the value of the largest field applied to saturate the sample. Such dependencies have indeed been observed in practice for some RE-TM thin film samples.[33]

C. Defects of type 3

Here, we assumed that the anisotropy constant K_u within the central region of the sample is only half the value of K_u elsewhere. All other parameters were the same as in the previous cases. The entire sample (including the defect) was initially magnetized along $+ Z$ and the system was allowed to relax and settle down into the remanent state. The various frames in Fig. 10 correspond to defects of different sizes and show the state of magnetization early on in the process of reversal, under an applied field which is only slightly above the computed coercive field. Frames (a)–
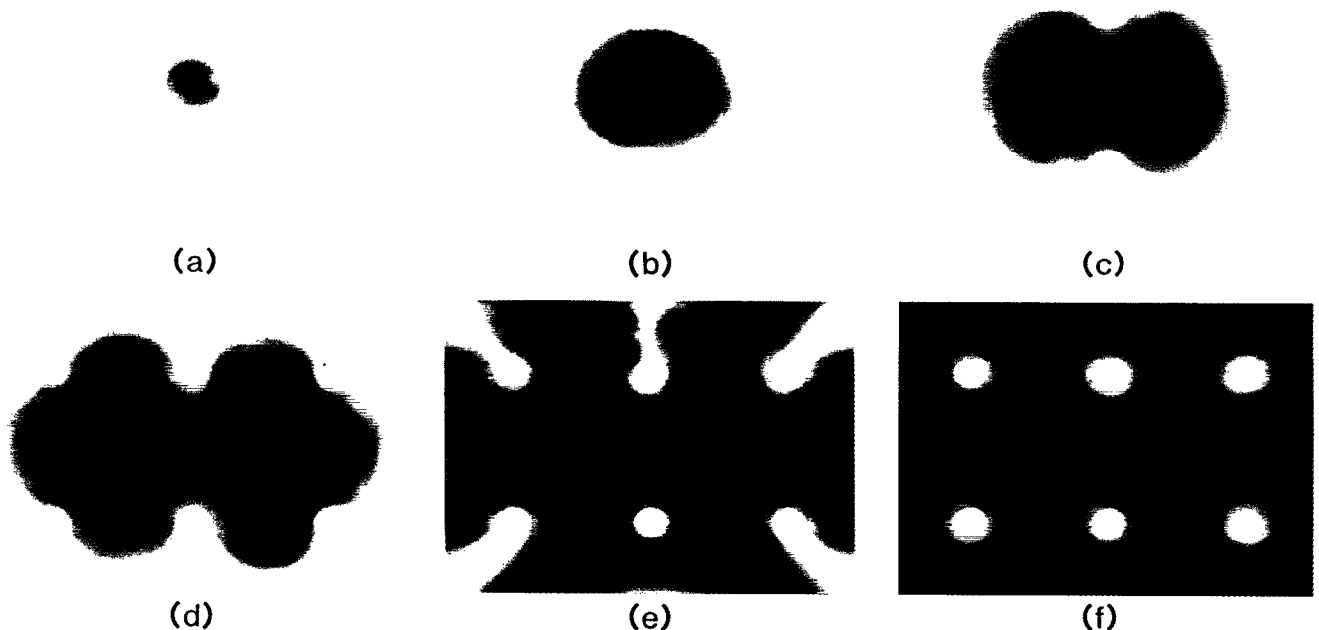

(a) (b) (c)

(d) (e) (f)

FIG. 9. Growth from a defect of the second type in the basic sample containing seven isolated regions of large anisotropy. Each region has diameter $D = 200$ Å and $K_u = 10^7$ erg/cm^3. The central defect was initially reverse magnetized and therefore constitutes a defect of type 2. The rest of the lattice was saturated along $+ Z$ and relaxed to the remanent state, as shown in frame (a). Frame (b) shows the state of the lattice under a reverse field of 3.5 kOe, which is only slightly above the coercivity for this sample. The remaining frames (c)–(f) follow the growth process in time and show how the magnetization fails to reverse in high K_u areas. The unreversed regions now become defects of the second type for future reversals.
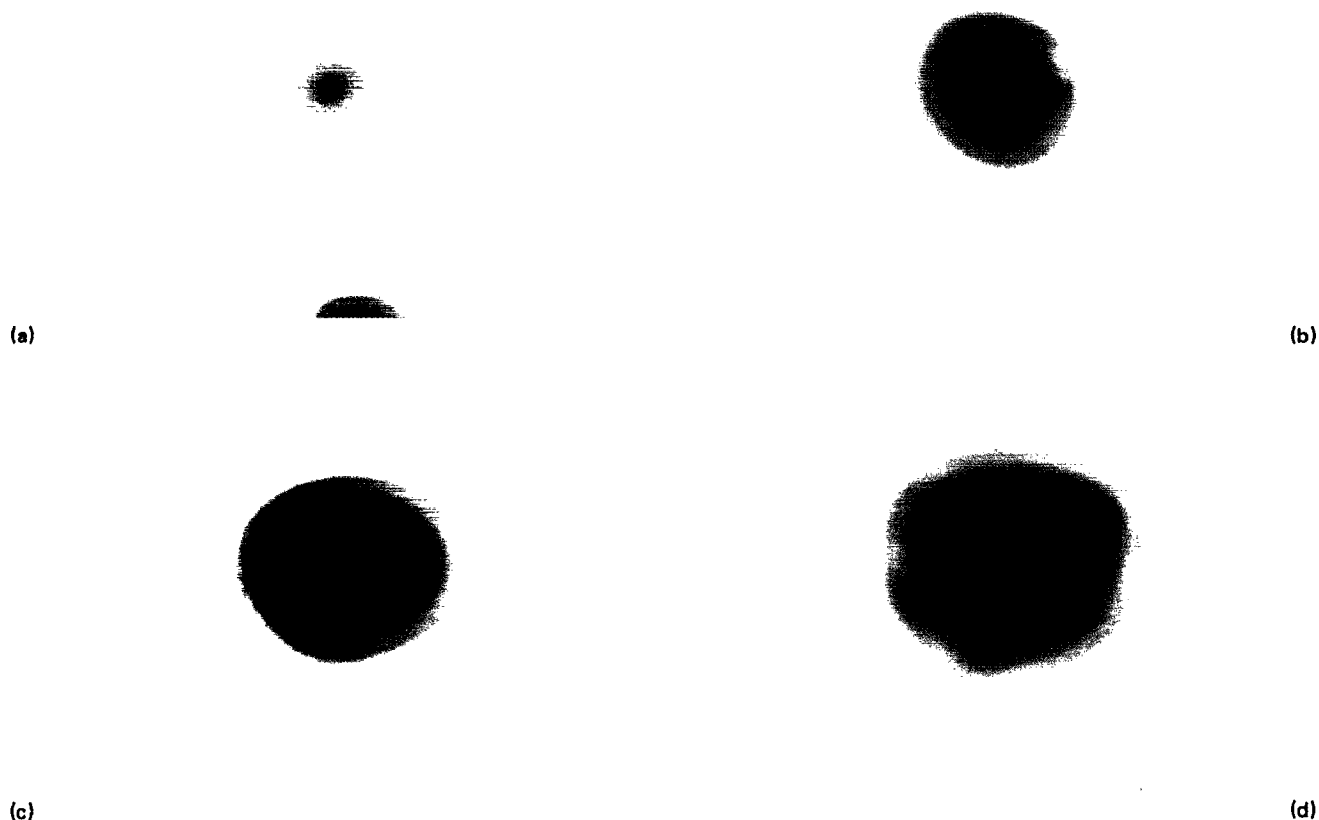
(a)

(b)

(c)

(d)

FIG. 10. Nucleation in the basic sample with defects of type 3 at the center of the lattice. The value of K_u within the defect is only half its value elsewhere. (a) Defect of diameter 200 Å under an applied field of 12.64 kOe. (b) Defect of diameter 600 Å subjected to the applied field of 11.75 kOe. (c) The defect diameter is 800 Å and the external field is 9.4 kOe. (d) The defect diameter is 1000 Å and the applied field is 8.7 kOe.

(d) correspond to defect diameters of $D = 200$, 600, 800, and 1000 Å, respectively. The corresponding coercive fields for these samples were computed as $H_c = 12.64$, 11.75, 9.4, and 8.7 kOe. Except for the 200 Å defect which does not help much in reducing coercivity [although one of the initial nuclei in frame (a) is centered on this defect], the other defects have an appreciable effect on the value of H_c and nucleation always begins at the defect.

D. Defects of type 4

In this type of defect the axes of anisotropy within the defective region are uniformly tilted away from the normal by a fixed angle. For several defects of this type the various frames of Fig. 11 show the states of the lattice both before and after nucleation. Except for the directions of local easy axes within the defects, all other parameters in these simulations were the same as before. Frames (a1) and (a2) in Fig. 11 correspond to a defect diameter of $D = 1000$ Å and a uniform tilt angle of 10° from normal within the defect. In (a1) the applied field is 12.32 kOe, which is just below coercivity, whereas in (a2) the applied field is 12.34 kOe. Compared to the basic sample with no defects, the coercivi-

ty has dropped only slightly, but the nucleation site is now on the boundary of the defect. Frames (b1) and (b2) correspond to a similar defect with a tilt angle of 20°. The coercive field in this case has dropped to 10.45 kOe. For a smaller defect of diameter 400 Å and 20° tilt angle, shown in frames (c1) and (c2), the coercivity was about 11.33 kOe. Apparently, in order to affect coercivity significantly, a defect of type 4 must be relatively large and have a substantial tilt angle.

The Stoner–Wohlfarth theory of magnetization reversal by coherent rotation[18] is applicable to this type of defect provided that the defect is not too small. A generalized version of this theory which includes the effects of demagnetization is described in the Appendix. It is shown in the Appendix that one of the preceding simulation results concerning a 1000 Å defect of type 4 with tilt angle of 20° is in good agreement with the theory.

II. STRUCTURE AND MOTION OF DOMAIN WALLS IN THE PRESENCE OF EXTERNAL AND/OR DEMAGNETIZING FIELDS

Having studied the process of nucleation in some detail, we now turn to the subject of domain wall structure and its associated coercivity. Figure 12 shows the structure of do-
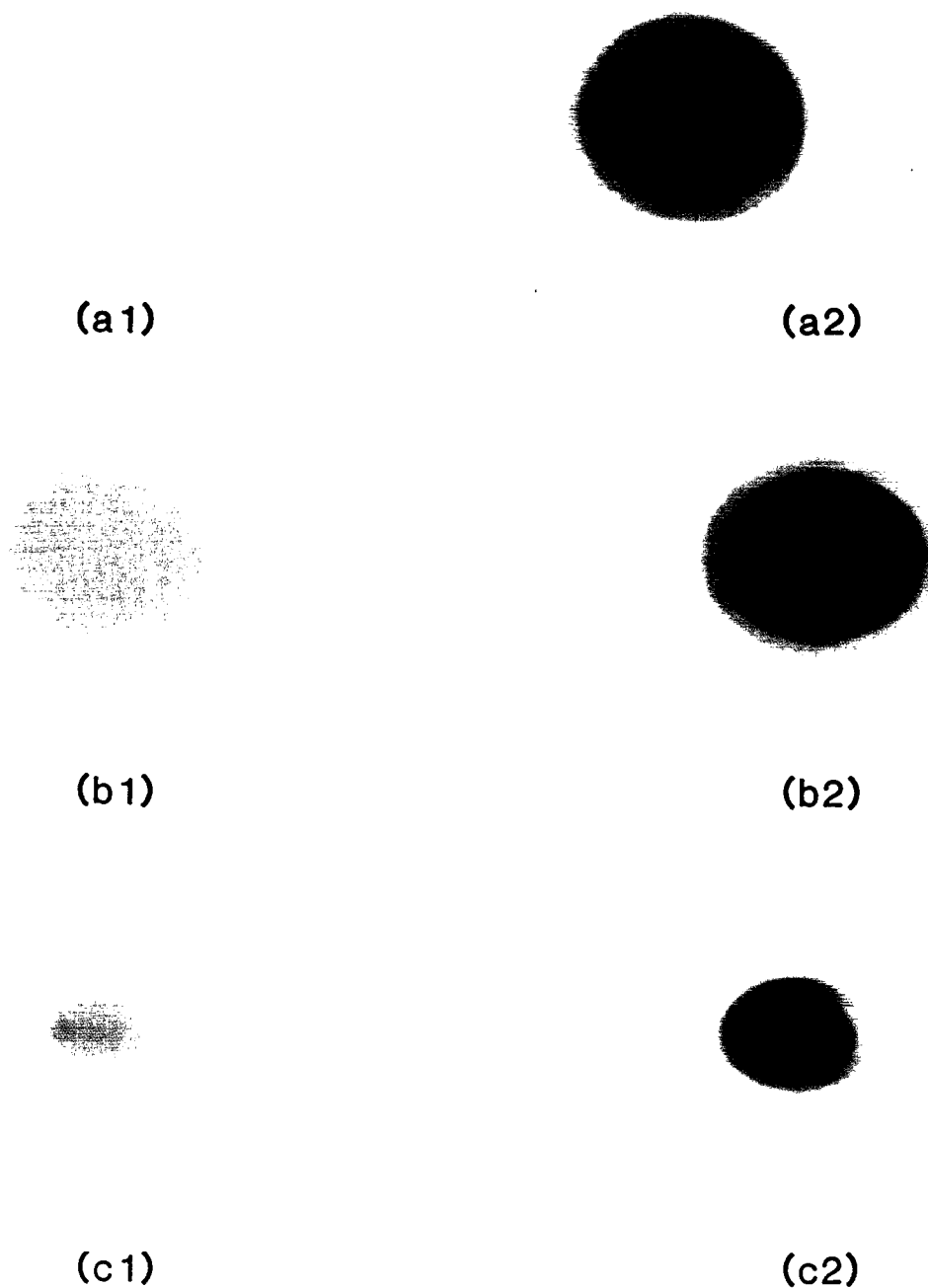
(a1)   **(a2)**

(b1)   **(b2)**

(c1)   **(c2)**

FIG. 11. Nucleation in the basic sample with defects of type 4. (a1) Defect with diameter of 1000 Å and anisotropy axis tilt of 10°, subject to an external field of 12.32 kOe. The defect is visible as the orange colored region in the center of the lattice. Although a red spot near the left boundary has formed at this stage, the applied field is not strong enough to reverse the magnetization of the sample. (a2) Same as (a1) but with an applied field of 12.34 kOe. The state shown in this frame is a snap shot of the reversal process. The nucleated domain continues to grow until the entire sample is reversed. (b1) Defect with diameter of 1000 Å and anisotropy axis tilt of 20°, subject to an applied field of 10.44 kOe. (b2) Same as (b1) but with an applied field of 10.46 kOe. This is a snap shot of the reversal process. (c1) Defect with diameter of 400 Å and anisotropy axis tilt of 20°, subject to an applied field of 11.32 kOe. (c2) Same as (c1) but with an applied field of 11.34 kOe. Again, this is a snap shot of the reversal process.

main walls in a medium with random axis anisotropy (cone angle $\Theta = 45°$) and with the same parameters as the basic sample. Initially the central band of the lattice was magnetized in the $+Z$ direction while the remaining part was magnetized in the $-Z$ direction, as shown in frame (a). When the lattice was allowed to relax for 0.8 ns, the pattern in frame (b) was obtained. Notice that there are three vertical Bloch lines (2π VBLs) in each wall and that the walls are no longer straight. By allowing the lattice to relax for another 0.9 ns we obtain the pattern of frame (c), which shows significant VBL movements along the walls. Finally, frame (d) shows the steady-state situation at $t = 4.56$ ns.
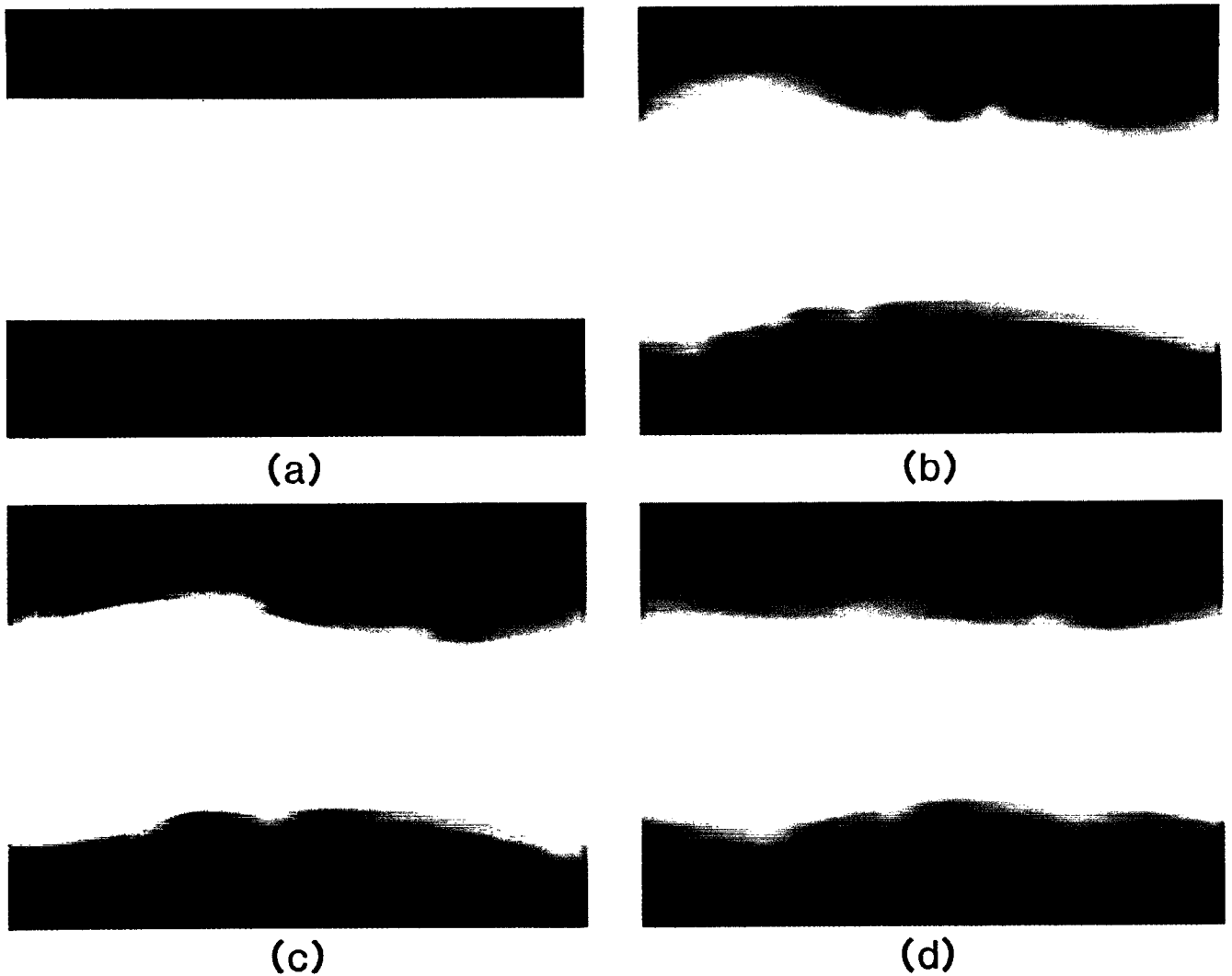
FIG. 12. Formation of domain walls in the basic sample with a cone angle of 45° and in the absence of an applied field. (a) Dipoles in the white region are initialized along $+ Z$, while dipoles in the dark region are initialized along $- Z$. (b) The state of the lattice at $t = 0.8$ ns. Each wall contains three vertical Bloch lines at this stage. (c) The state of the lattice at $t = 1.7$ ns. The number of VBLs has not changed since the previous frame, but they have moved along the walls. (d) The steady state of the lattice at $t = 4.56$ ns. The number of VBLs in each wall is still 3.

Both walls are now straightened considerably, but the number of VBLs in each wall has not changed; no amount of relaxation can unwind a 2π Bloch line.

The curves in Fig. 13 show average magnetization $\langle M_z \rangle$ and total energy E_{tot} of the system during the relaxation process which was depicted in the previous figure. The inset in Fig. 13(b) shows the various components of energy. Obviously, the demagnetization energy does not change much during the process of wall formation. This result should be expected since, in this particular example, film thickness h is several times greater than the wall thickness. On the other hand, anisotropy energy drops sharply in the early phase as the moments throughout the lattice move closer to the local easy axes. In fact, this reduction is large enough to overwhelm the modest increase in the anisotropy energy at the walls. For the same reasons the exchange energy of the entire system rises, albeit very slightly, despite a sharp reduction of the exchange energy at the walls.

A perpendicular field $H_z = - 200$ Oe moves the two walls in Fig. 12(d) somewhat closer to each other, but fails to eliminate the stripe of reverse magnetization. The steady state of the lattice under this applied field is shown in Fig. 14. The corresponding curves of $\langle M_z \rangle$ and E_{tot} in Fig. 15
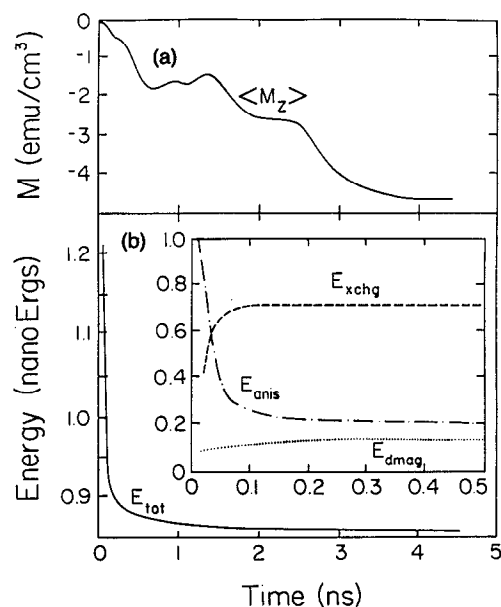

FIG. 13. Plots of average magnetization and energy in the process of domain wall formation corrresponding to Fig. 12. (a) $\langle M_z \rangle$ versus time. (b) Total energy of the lattice versus time. The inset shows the evolution of exchange, anisotropy, and demagnetization energies during the initial phase of the process.
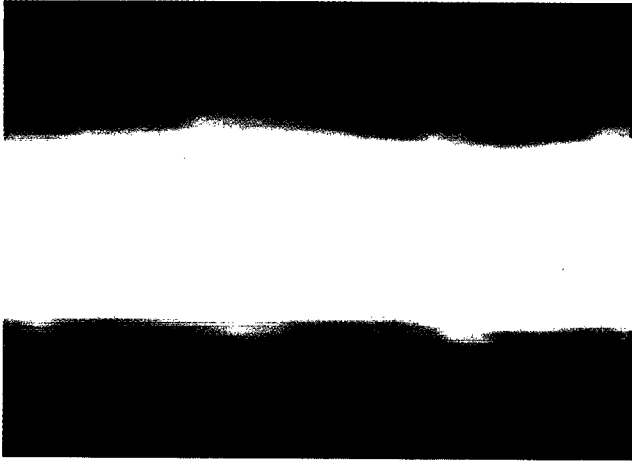
FIG. 14. Steady state of the lattice (shown here at $t = 3.66$ ns) when the stripe domain of Fig. 12(d) is subjected to an external field $H_z = -200$ Oe.

FIG. 15. Plots of average magnetization and energy when the stripe domain of Fig. 12(d) shrinks under an external field $H_z = -200$ Oe.

indicate that the time needed to arrive at the steady state is about 2 ns. In this experiment, the force of demagnetization opposes the external field in collapsing the reverse-magnetized stripe.

The stripe domain shown in Fig. 12(d) will collapse under the applied field of $H_z = -1000$ Oe, as shown in Fig. 16. Frames (a) and (b) in this figure correspond to $t = 0.96$ ns and $t = 3.58$ ns, respectively. The curves of $\langle M_z \rangle$ and E_{tot} in Fig. 17 show the rate of reduction of the average magnetization and energy during this collapse process.

In the remaining investigations we used a different set of parameters for the lattice. These parameters were: $M_s = 175$ emu/cm^3, $K_u = 0.5 \times 10^6$ erg/cm^3, $A_x = 0.5 \times 10^{-7}$ erg/cm, and cone angle $\Theta = 20°$. In one simulation experiment we initialized the state of magnetization randomly, with each dipole moment being equally likely to be set either parallel or antiparallel to the Z axis. After about 900 steps (corresponding to 5 ps) in which the state of the lattice was relaxed following the LLG equation,
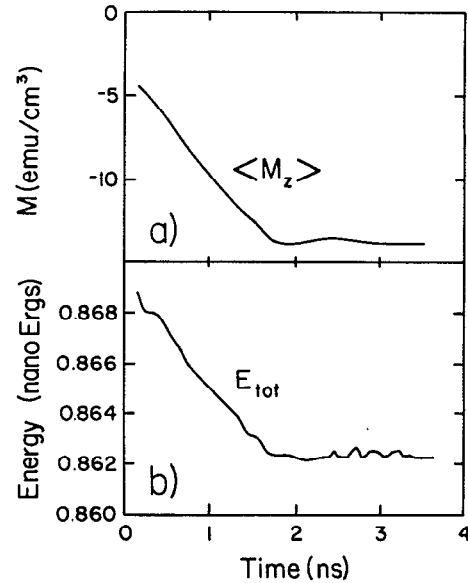
the system arrived at the state shown in frame (a) of Fig. 18. Small domains had clearly formed at this stage, but the system was far from equilibrium. Twenty-thousand iterations and 1.2 ns later, the system arrived at the equilibrium state shown in frame (b). The final state is demagnetized with stripe domains containing several vertical Bloch lines in their walls. This experiment is similar to rapid cooling of a real sample in zero field from above the Curie point to the room temperature.

In another simulation experiment we applied a reverse external field of 3.16 kOe (just above coercivity) to initiate the reversal. Once the nuclei had formed, the field was reduced to zero and the domains were left to themselves to
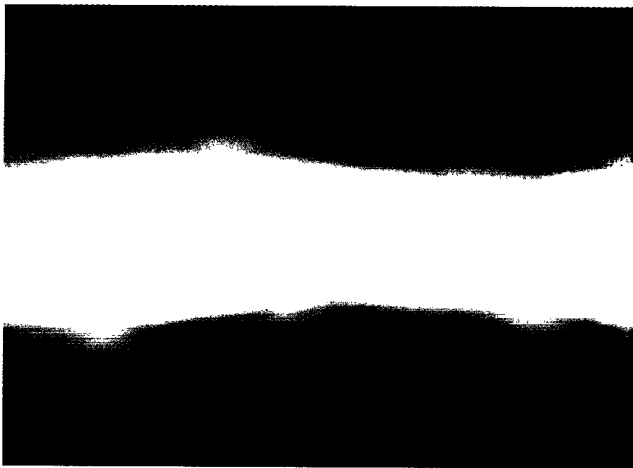
(a)
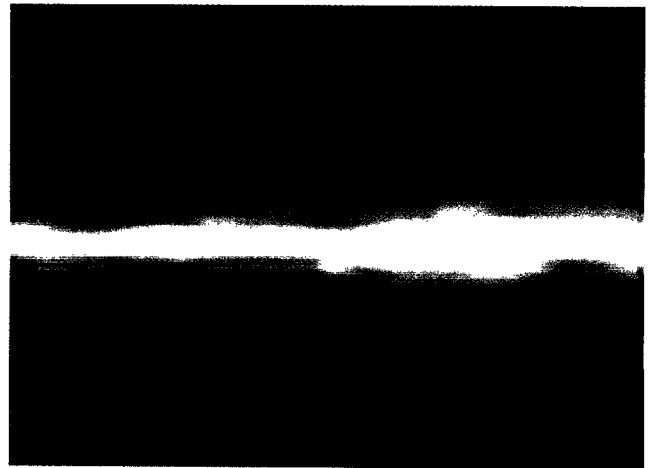
(b)

FIG. 16. Collapse of the stripe domain of Fig. 12(d) under an external field $H_z = -1000$ Oe. Frames (a) and (b) show the state of the lattice at $t = 0.96$ ns and $t = 3.58$ ns, respectively.
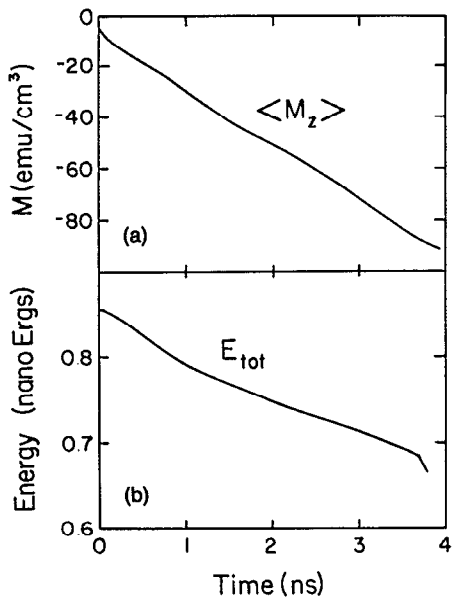
FIG. 17. Plots of average magnetization and energy when the stripe domain of Fig. 12(d) collapses under an external field $H_z = -1000$ Oe.

frames (d) and (e). Eventually, the small domain disappears and the lattice reaches equilibrium as shown in frame (f). Figure 20(a) shows the average lattice magnetization $\langle M_z \rangle$ versus time for this experiment. The initial sharp drop in $\langle M_z \rangle$ occurs when the early nuclei merge and expand. The plateau corresponds to the time during which one domain expands at the expense of the other. At the end of the plateau, the sudden collapse of the small domain (similar to a bursting bubble) causes a rapid drop in $\langle M_z \rangle$. Soon afterwards the magnetization reaches an equilibrium value near zero, and the lattice begins to stabilize. The plot of energy versus time in Fig. 20(b) shows a similar behavior. The inset in Fig. 20 shows the various contributions to energy, namely, the energies due to exchange, anisotropy, and demagnetization. Note how the burst of the small bubble, at around $t = 23$ ns, causes the demagnetizing energy to rise, while at the same time both exchange and anisotropy energies (which are associated with domain walls) drop.

develop under the pressure of the wall energy and the demagnetizing force. The various frames of Fig. 19 show several states of this development. In frame (a) the field has just been turned off, leaving behind three nuclei that are clearly visible in the picture. Since the force of demagnetization for this sample is larger than that of the wall energy, the nuclei expand and eventually cause the sample to demagnetize. First the two nuclei in the lower part of the frame merge; then the remaining domains expand as shown in frames (b) and (c). Soon, however, the larger domain begins to push the smaller one toward collapse, as shown in

III. CONCLUDING REMARKS

Several hypothetical mechanisms of coercivity in thin films of amorphous rare earth-transition metal alloys were examined in this paper. Using computer simulations, we found that regions as small as a few hundred angstroms in diameter with unusually large or small magnetic parameters could act as nucleation centers and initiate the reversal process. Values of the coercive field obtained by simulation are comparable to those observed in practice. Whether or not these hypothetical sources exist in real materials is a question whose answer must await further progress in experimental "nanomagnetics." Among the existing tools for observation of the magnetic state in thin films, Lorentz electron microscopy[34] and magnetic force microscopy[35] have the potential to clarify the situation in the near future.
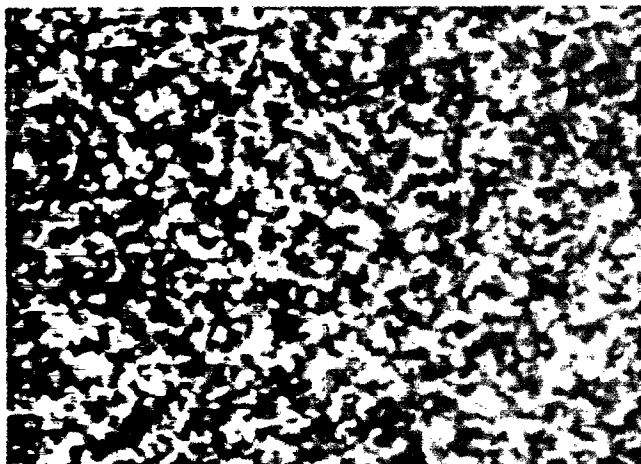
(a)

(b)

FIG. 18. Relaxation of the lattice starting from a random initial state and in the absence of an applied field. The parameters for this simulation are: $M_s = 175$ emu/cm³, $K_u = 0.5 \times 10^6$ erg/cm³, $A_x = 0.5 \times 10^{-7}$ erg/cm, $h = 500$ Å, $\alpha = 0.5$, $\gamma = -10^7$ Hz/Oe, and cone angle $\Theta = 20°$. (a) The state of the lattice at $t = 5.06$ ps. (b) The state of the lattice at $t = 1.2$ ns.
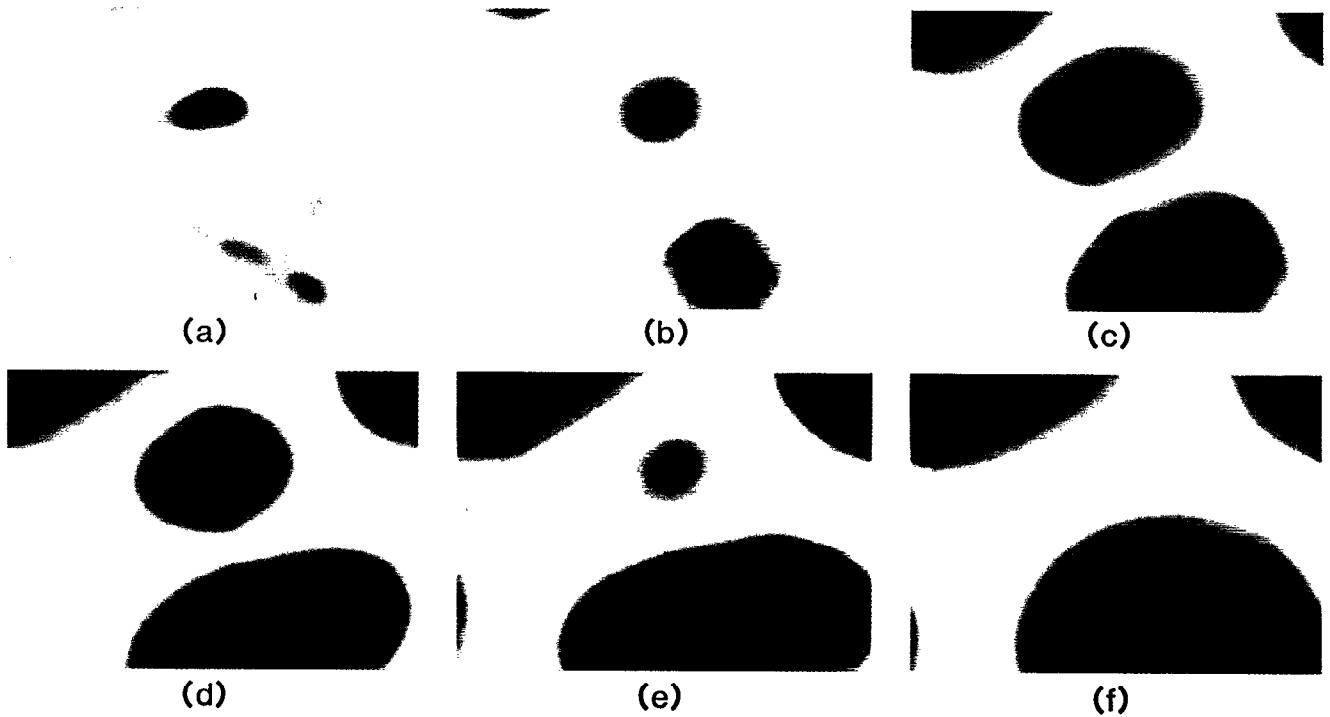
FIG. 19. Demagetization in the absence of an applied field, for a sample with the same set of parameters as in Fig. 18. The sample is initially saturated, then briefly exposed to an external field of 3.16 kOe in order to create several small nuclei. The field is then turned off and the domains allowed to evolve under internal forces. (a) The state of the lattice immediately after the external field has been turned off. (b) The situation at $t = 1$ ns. The two nuclei in the lower part of frame (a) have merged. (c) The state of magnetization of the lattice at $t = 5$ ns. The domain in the center of the frame has now reached its maximum size and, from now on, it will shrink. (d) At $t = 20$ ns. The small domain in the center is shrinking, while the big domain continues to expand. (e) At $t = 24$ ns the small central domain is about to burst. (f) The final state. The domain is now steady and the net magnetization of the lattice is close to zero.
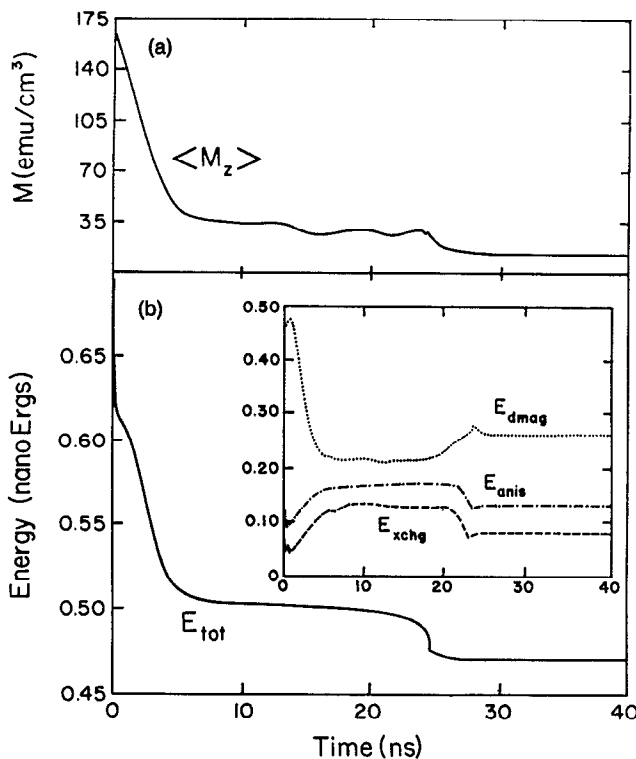

FIG. 20. Plots of average magnetization and energy during the relaxation process described in Fig. 19. (a) $\langle M_z \rangle$ versus time. (b) Average energy of the lattice and its various components versus time.

ACKNOWLEDGMENTS

APPENDIX

The theory of magnetization reversal by coherent rotation was developed by Stoner and Wohlfarth in the context of elongated fine particles.[36] Their theory has since been adapted and applied to reversal in thin films.[37–39] In this appendix we generalize the Stoner–Wohlfarth theory to account for the demagnetizing effects in thin films. The results will then be applied to the basic sample with defects of type 4 (see Sec. I) in order to determine the dependence of coercivity on the tilt angle.

Consider a uniform film with magnetization M_s and anisotropy energy constant K_u, as shown in Fig. 21. The axis of anisotropy makes angle Θ_A with the Z axis, and assuming that the magnetization processes are coherent, we denote by Θ_M the angle between the magnetization vector and Z. The applied field H_{ext} is also uniform and its angle with Z is denoted by Θ_H. All angles are to be measured clockwise from the positive Z axis, as indicated in the figure. The question we are about to address is the following: For a fixed set of values of $K_u, \Theta_A, M_s,$ and Θ_H, how does the angle Θ_M vary with the magnitude of the applied field H_{ext}? In particular, what is the equilibrium value of
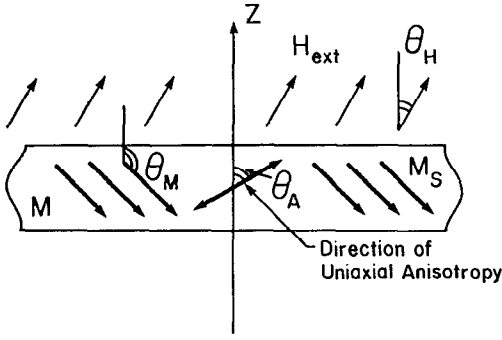
FIG. 21. Cross-sectional view of a thin magnetic film with uniaxial anisotropy and uniform magnetization under an externally applied field H_{ext}. All angles are measured clockwise from the positive Z axis. M_s is the saturation magnetization of the film and its angle with Z is denoted by Θ_M. The angle of the applied field with Z is Θ_H, while the angle between Z and the axis of anisotropy is Θ_A. The field, the magnetization, the axis of anisotropy, and the Z axis are coplanar.

Θ_M when $H_{\text{ext}} = 0$, and how does Θ_M change as H_{ext} increases from zero to infinity in the fixed direction given by Θ_H?

To answer the above question, we consider the magnetic energy E_m of the system consisting of the external field energy, the demagnetizing energy, and the anisotropy energy, as follows:

$$E_m = -M_s H_{\text{ext}} \cos(\Theta_M - \Theta_H) + 2\pi M_s^2 \cos^2 \Theta_M + K_u \sin^2(\Theta_M - \Theta_A). \tag{A1}$$

The second and third terms in Eq. (A1) can be combined to yield,

$$E_m = -M_s H_{\text{ext}} \cos(\Theta_M - \Theta_H) + \tfrac{1}{2}(K_u + 2\pi M_s^2)$$
$$- \sqrt{(K_u/2)^2 - \pi M_s^2 K_u \cos(2\Theta_A) + (\pi M_s^2)^2}$$
$$\times \cos\left[2\Theta_M - \tan^{-1}\left(\frac{K_u \sin(2\Theta_A)}{K_u \cos(2\Theta_A) - 2\pi M_s^2}\right)\right]. \tag{A2}$$

Next we define an effective internal field H_{eff} and its associated angle Θ_{eff} as follows:

$$H_{\text{eff}} = \sqrt{(2K_u/M_s)^2 - 16\pi K_u \cos(2\Theta_A) + (4\pi M_s)^2}, \tag{A3}$$

$$\Theta_{\text{eff}} = \frac{1}{2} \tan^{-1}\left(\frac{(2K_u/M_s)\sin(2\Theta_A)}{(2K_u/M_s)\cos(2\Theta_A) - 4\pi M_s}\right). \tag{A4}$$

In evaluating Θ_{eff} from Eq. (A4) it is imperative that one take into consideration the signs of both the numerator and the denominator of the arctangent's argument. The value thus obtained for the arctangent should be somewhere in the interval between 0 and 2π, resulting in a value of Θ_{eff}

between 0 and π. Note that both Θ_{eff} and H_{eff} are constants, depending only on the internal parameters of the film M_s, K_u, and Θ_A. Later, we will show that in the absence of an external field, the equilibrium orientation of magnetization is along the direction of this effective field.

Using the above definitions for H_{eff} and Θ_{eff}, one can rewrite the expression for energy in Eq. (A2) as

$$E_m = \tfrac{1}{2}(K_u + 2\pi M_s^2) - M_s H_{\text{ext}} \cos(\Theta_M - \Theta_H)$$
$$- \tfrac{1}{4} M_s H_{\text{eff}} \cos[2(\Theta_M - \Theta_{\text{eff}})]. \tag{A5}$$

Since H_{eff} and Θ_{eff} are constants, independent of the magnitude and the direction of the applied field, one defines the relative values of Θ_M, Θ_H, and H_{ext} as follows:

$$\widehat{\Theta}_M = \Theta_M - \Theta_{\text{eff}}, \tag{A6}$$

$$\widehat{\Theta}_H = \Theta_H - \Theta_{\text{eff}}, \tag{A7}$$

$$\widehat{H}_{\text{ext}} = H_{\text{ext}}/H_{\text{eff}}. \tag{A8}$$

In terms of these relative parameters, Eq. (A5) is now written

$$E_M = \tfrac{1}{2}(K_u + 2\pi M_s^2) - \tfrac{1}{2} M_s H_{\text{eff}}\left[2\widehat{H}_{\text{ext}} \cos(\widehat{\Theta}_M - \widehat{\Theta}_H)\right.$$
$$\left. + \tfrac{1}{2}\cos(2\widehat{\Theta}_M)\right]. \tag{A9}$$

The problem is now reduced to finding the equilibrium value of $\widehat{\Theta}_M$ as a function of $\widehat{H}_{\text{ext}}$ for a fixed value of $\widehat{\Theta}_H$. To this end, we differentiate E_m with respect to $\widehat{\Theta}_M$, and set the derivative equal to zero in order to find the minima and maxima of the energy function. We find

$$\frac{\partial E_m}{\partial \widehat{\Theta}_M} = \frac{1}{2} M_s H_{\text{eff}}\left[2\widehat{H}_{\text{ext}} \sin(\widehat{\Theta}_M - \widehat{\Theta}_H) + \sin(2\widehat{\Theta}_M)\right]. \tag{A10}$$

Aside from an irrelevant constant coefficient, the right-hand side of Eq. (A10) contains the following sinusoidal functions:

$$F(\widehat{\Theta}_M) = 2\widehat{H}_{\text{ext}} \sin(\widehat{\Theta}_M - \widehat{\Theta}_H), \tag{A11}$$

$$G(\widehat{\Theta}_M) = -\sin(2\widehat{\Theta}_M). \tag{A12}$$

Figure 22 shows plots of these functions with $\widehat{\Theta}_H$ arbitrarily set to 45°, with several values of $\widehat{H}_{\text{ext}}$ chosen from 0 to 1 in steps of 0.1. For given values of $\widehat{H}_{\text{ext}}$ and $\widehat{\Theta}_H$, the curves $F(\widehat{\Theta}_M)$ and $G(\widehat{\Theta}_M)$ cross in at most four points, at which points the derivative of E_m is zero. To determine those crossing points that correspond to actual minima of energy, we note in Fig. 22 that as one moves from the left to the right of a crossing point corresponding to a minimum, the slope of E_m, which is proportional to $F(\Theta) - G(\Theta)$, goes from a negative value to zero, then to a positive value. In other words, before the crossing point $F(\Theta)$ must be less than $G(\Theta)$, whereas after the crossing point $F(\Theta)$ must be greater than $G(\Theta)$. Those crossing points that satisfy this criterion are marked with a small circle in Fig. 22.

At $\widehat{H}_{\text{ext}} = 0$ there are always two stable values for $\widehat{\Theta}_M$, namely, 0 and 180°, corresponding to $\Theta_M = \Theta_{\text{eff}}$ and
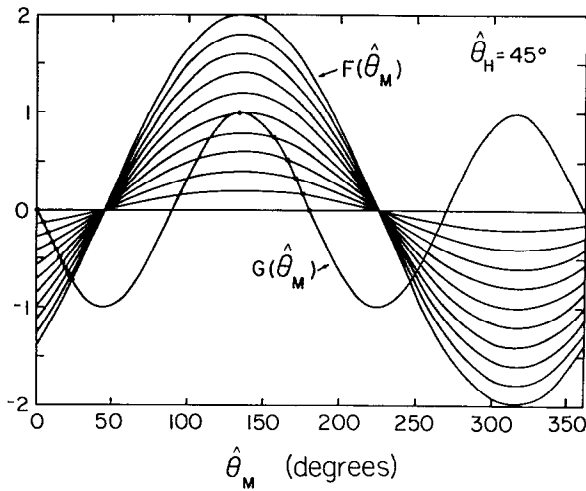
FIG. 22. Plots of the functions $F(\hat{\Theta}_M)$ and $G(\hat{\Theta}_M)$ defined in Eqs. (A11) and (A12). The various $F(\hat{\Theta}_M)$ shown here have $\hat{\Theta}_H = 45°$ and $\hat{H}_{ext} = 0$ to 1 in steps of 0.1. The points $\hat{\Theta}_M$ at which $F(\hat{\Theta}_M)$ crosses $G(\hat{\Theta}_M)$ from below the figure correspond to minima of energy E_m. These crossing points are identified on the figure with small circles o.

$\Theta_M = \Theta_{eff} + 180°$. For the situation depicted in Fig. 22, $\Theta_H = 45°$, that is, $\Theta_H = \Theta_{eff} + 45°$. Now, if the system happens to be in the stable state with $\Theta_M = \Theta_{eff}$ when the applied field is zero, then, as $\hat{H}_{ext}$ increases, the crossing point moves toward larger values of $\hat{\Theta}_M$ until it reaches $\Theta_M = \Theta_H = 45°$ for infinitely large $\hat{H}_{ext}$. On the other hand, if originally $\Theta_M = \Theta_{eff} + 180°$, then, as $\hat{H}_{ext}$ increases, Θ_M decreases until it reaches a critical value of $\hat{\Theta}_C = 135°$ at the critical field value of $\hat{H}_C = 0.5$. At the critical point, the minimum state of energy in which the system has been residing becomes a saddle point. Further increases in $\hat{H}_{ext}$ eliminate this minimum, forcing the system to jump to the only remaining state of minimum energy which, in the case of Fig. 22, is at $\hat{\Theta}_M = 15°$. After the jump, $\hat{\Theta}_M$ increases continuously with increasing $\hat{H}_{ext}$, asymptotically approaching $\Theta_H = 45°$.

Qualitatively, the behavior just described for the case of $\hat{\Theta}_H = 45°$ applies to all other values of $\hat{\Theta}_H$ as well, but the values of the critical field $\hat{H}_C$ and the critical angle $\hat{\Theta}_C$ will depend on the exact value of $\hat{\Theta}_H$, of course. To determine these critical parameters one notes that at the critical point the two curves $F(\Theta)$ and $G(\Theta)$ become tangent to each other, that is,

$$F(\hat{\Theta}_C) = G(\hat{\Theta}_C), \qquad (A13a)$$

$$F'(\hat{\Theta}_C) = G'(\hat{\Theta}_C). \qquad (A13b)$$

Solving these equations, one obtains

$$\tan \hat{\Theta}_C = -(\tan \hat{\Theta}_H)^{1/3}, \qquad (A14)$$

$$\hat{H}_C = -\cos^3 \hat{\Theta}_C / \cos \hat{\Theta}_H. \qquad (A15)$$

Now, assuming that the equilibrium state in the absence of the external field occurs at $\hat{\Theta}_M = 0$, there exist only two possibilities. In the first instance $0 \leqslant \hat{\Theta}_H \leqslant 90°$, in which case $\hat{\Theta}_M$ increases continuously toward $\hat{\Theta}_H$ with increasing H_{ext}; no critical fields will be reached in this case and no discontinuous jumps will occur. In the second instance $90° \leqslant \hat{\Theta}_H \leqslant 180°$. In this case $\hat{\Theta}_M$ initially increases with $\hat{H}_{ext}$ until it reaches $\hat{\Theta}_C$ at $\hat{H}_{ext} = \hat{H}_C$. At the critical field $\hat{\Theta}_M$ jumps to the other side and suddenly becomes greater than $\hat{\Theta}_H$. The process then resumes its continuous nature, with $\hat{\Theta}_M$ asymptotically approaching $\hat{\Theta}_H$.

As an example, consider the following set of parameters corresponding to a defect of type 4 studied in Sec. I: $K_u = 10^6$ erg/cm^3, $\Theta_A = 20°$, $M_s = 100$ emu/cm^3, and $\Theta_H = 180°$. From Eq. (A3) we find $H_{eff} = 19.055$ kOe and, from Eq. (A4), $\Theta_{eff} = 21.215°$. Thus $\hat{\Theta}_H = 158.785°$, resulting in $\hat{\Theta}_C = 36.11°$ and $\hat{H}_C = 0.566$. The critical (i.e., switching) field is thus given by $H_{ext} = H_{eff} \times \hat{H}_C = 10.78$ kOe, in good agreement with the value of 10.45 kOe which was arrived at numerically in Sec. I for a 1000 Å defect.

Figure 23 shows several hysteresis loops for a thin film sample with $K_u = 10^6$ erg/cm^3 and $M_s = 100$ emu/cm^3.
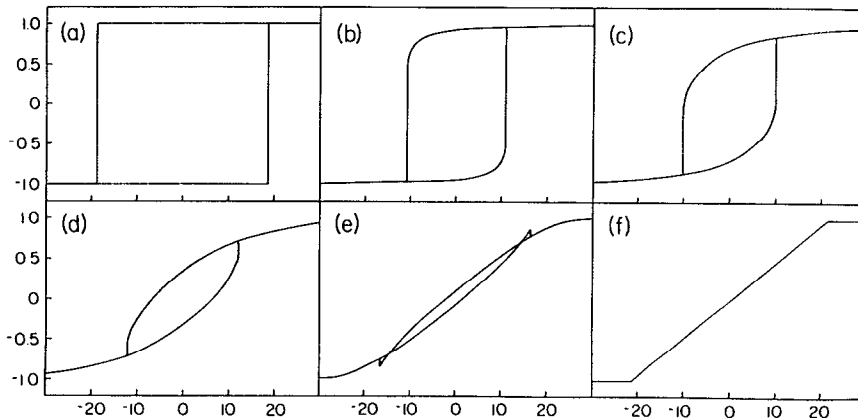

FIG. 23. Calculated hysteresis loops for a thin film sample according to the Stoner–Wohlfarth theory, including the effects of demagnetization. The external field is parallel to Z, the film parameters are $M_s = 100$ emu/cm^3 and $K_u = 10^6$ erg/cm^3, and the loops in (a)–(f) correspond to $\Theta_A = 0°, 20°, 45°, 70°, 85°,$ and $90°$, respectively.

The external field is assumed to be along the Z axis, that is $\Theta_H = 0°$ or $180°$. The values of Θ_A corresponding to different loops in Fig. 23 are $0°$, $20°$, $45°$, $70°$, $85°$, and $90°$. When $\Theta_A = 0°$ we find from Eq. (A4) that $\Theta_{\text{eff}} = 0°$ provided that $K_u > 2\pi M_s^2$, which happens to be the case here. We also find $H_{\text{eff}} = 2K_u/M_s - 4\pi M_s = 18.744$ kOe from Eq. (A3). From Eqs. (A14) and (A15) one finds $\Theta_C = 0°$ and $H_C = 1$, leading to a perfectly square loop with a coercivity of 18.744 kOe, as shown in the figure. The lowest value of coercivity is around 10 kOe, and is reached when $\Theta_A \simeq 45°$. The loop at $\Theta_A = 85°$ has a curious shape: The jump in Θ_M has caused a drop (rather than an increase) in the Z-component of magnetization. Finally, for $\Theta_A = 90°$ we have $\Theta_{\text{eff}} = 90°$ and $H_{\text{eff}} = 2K_u/M_s + 4\pi M_s = 21.256$ kOe. In this case there are no jumps but there is a discontinuity of slope at $H_{\text{ext}} = H_{\text{eff}}$, where the magnetization comes into alignment with the direction of the applied field.

REFERENCES

1. P. Hansen and H. Heitmann, IEEE Trans. Magnet. **25**, 4390 (1989).
2. P. Chaudhari, J. J. Cuomo, and R. J. Gambino, Appl. Phys. Lett. **22**, 337 (1973).
3. R. J. Gambino, P. Chaudhari, and J. J. Cuomo, AIP Conf. Proc. **18** (1), 578–592 (1973).
4. T. Chen, D. Cheng, and G. B. Charlan, IEEE Trans. Magnet. **16**, 1194 (1980).
5. Y. Mimura, N. Imamura, and T. Kobayashi, IEEE Trans. Magnet. **12**, 779 (1976).
6. Y. Mimura, N. Imamura, T. Kobayashi, A. Okada, and Y. Kushiro, J. Appl. Phys. **49**, 1208 (1978).
7. F. E. Luborsky, J. Appl. Phys. **57**, 3592 (1985).
8. H. Tsujimoto, M. Shouji, A. Saito, S. Matsushita, and Y. Sakurai, J. Magnet. Magnet. Mat. **35**, 199 (1983).
9. G. A. N. Connell, R. Allen, and M. Mansuripur, J. Appl. Phys. **53**, 7759 (1982).
10. M. Urner-Wille, P. Hansen, and K. Witter, IEEE Trans. Magnet. **16**, 1188 (1980).
11. T. C. Anthony, J. Burg, S. Naberhuis, and H. Birecki, J. Appl. Phys. **59**, 213 (1986).
12. Y. Sakurai and K. Onishi, J. Magnet. Magnet. Mat. **35**, 183 (1983).
13. R. Harris, M. Plischke, and M. J. Zuckermann, Phys. Rev. Lett. **31**, 160 (1973).
14. R. Harris, S. H. Sung, and M. J. Zuckermann, IEEE Trans. Magnet. **14**, 725 (1978).
15. R. Friedberg and D. I. Paul, Phys. Rev. Lett. **34**, 1234 (1975).
16. D. I. Paul, Phys. Lett. A **64**, 485 (1978).
17. D. I. Paul, J. Appl. Phys. **53**, 2362 (1982).
18. B. K. Middelton, "Magnetic Thin Films and Devices," in *Active and Passive Thin Film Devices*, edited by T. J. Coutts (Academic, New York, 1978), Chap. 11.
19. A. Sukiennicki and E. Della Torre, J. Appl. Phys. **55**, 3739 (1984).
20. K. Ohashi, H. Tsuji, S. Tsunashima, and S. Uchiyama, Jpn. J. Appl. Phys. **19**, 1333 (1980).
21. K. Ohashi, H. Takagi, S. Tsunashima, S. Uchiyama, and T. Fujii, J. Appl. Phys. **50**, 1611 (1979).
22. M. C. Chi and R. Alben, J. Appl. Phys. **48**, 2987 (1977).
23. J. M. D. Coey, J. Appl. Phys. **49**, 1646 (1978).
24. J. M. D. Coey and D. H. Ryan, IEEE Trans. Magnet. **20**, 1278 (1984).
25. E. Callen, Y. J. Liu, and J. R. Cullen, Phys. Rev. B **16**, 263 (1977).
26. R. C. O'Handley, J. Appl. Phys. **62**, R15 (1987).
27. M. Mansuripur and R. Giles, Comput. Phys. **4**, 291 (1990).
28. M. Mansuripur, J. Appl. Phys. **63**, 5809 (1988).
29. M. Mansuripur and T. W. McDaniel, J. Appl. Phys. **63**, 3831 (1988).
30. M. Mansuripur and R. Giles, IEEE Trans. Magnet. **24**, 2326 (1988).
31. M. Mansuripur, J. Appl. Phys. **66**, 3731 (1989).
32. M. Mansuripur and M. F. Ruane, IEEE Trans. Magnet. **22**, 33 (1986).
33. P. Wolniansky, S. Chase, R. Rosenvold, M. Ruane, and M. Mansuripur, J. Appl. Phys. **60**, 346 (1986).
34. C. J. Lin and D. Rugar, IEEE Trans. Magnet. **24**, 2311 (1988).
35. D. Rugar, H. J. Mamin, and P. Guthner, Appl. Phys. Lett. **55**, 2588 (1989).
36. E. C. Stoner and E. P. Wohlfarth, Phil. Trans. R. Soc. A **240**, 599 (1948).
37. D. O. Smith, J. Appl. Phys. **29**, 264 (1958).
38. E. M. Bradley and M. Prutton, J. Electron. Control **6**, 81 (1959).
39. S. Middelhoek, Ph.D. thesis, University of Amsterdam, 1961.